Remote Sensing-based Investigation of historical Land Surface Temperature Responses to Intense Land Cover Change

Amin Naboureh[1], Meysam Moharrami[2*], Sara Attarchi[2], Seyed Kazem Alavipanah[2]

[1] Research Center for Digital Mountain and Remote Sensing Application, Institute of Mountain Hazards and Environment, Chinese Academy of Sciences, Chengdu, China, 610041.
[2] Department of Remote Sensing and GIS, Faculty of Geography, University of Tehran, Tehran, Iran

Keywords: Remote Sensing; Land Surface Temperature; Land Cover Change; Environmental costs; China

Abstract

Rapid urbanization and agricultural expansion have dramatically intensified land cover change (LCC) in Chengdu City, China, over the past three decades. This study investigates the interaction between LCC and land surface temperature (LST) from 1990 to 2020 using satellite remote sensing data in combination with cloud computing, machine learning, and reference data migration. A consistent time-series of land cover maps at 30 m resolution was generated for four benchmark years (1990, 2000, 2010, and 2020). The maps achieved an average overall accuracy of 91% and F1-scores exceeding 85% across all classes, confirming the robustness of the classification. The results reveal pronounced LCC driven primarily by agricultural expansion and urban growth. LST analysis showed substantial temporal variability, with mean temperatures stable between 1990 and 2000 (26.27 °C), rising sharply by 2010 (31.86 °C), and declining to 23.69 °C by 2020. Zonal statistics demonstrated strong relationships between LC and LST: bare land (32.49 °C) and built-up areas (28.21 °C) exhibited the highest mean LSTs, whereas forests (21.20 °C) and water bodies (20.33 °C) acted as significant cooling elements. Overall, this study underscores the critical role of LCC in shaping Chengdu's thermal environment. The results provide new insights into the coupled processes of urbanization, agricultural intensification, and climate variability, while demonstrating a robust and scalable framework for LC monitoring to support sustainable urban and environmental planning.

1. Introduction

Land Cover (LC) generally defines as the various physical or biological forms of cover that exist on the earth's surface, such as agricultural land, grasslands, and forests (Gómez et al., 2016; Mohammadi Foumani et al., 2024). Over the past decades, Land cover change (LCC) has intensified worldwide due to human activities and climate change (Naboureh et al., 2021; He et al., 2025). These changes affect terrestrial ecosystems, water cycles, and local to regional climate regulation (Ebrahimy et al., 2022). Among the many impacts of LCC, land surface temperature (LST) variations are particularly important, as they significantly impact urban heat island effect, energy balance alterations, and environmental sustainability challenges (Firozjaei et al., 2018; Komeh et al., 2025).

Urban areas in China have been experiencing dramatic LCC over recent decades, reflecting unprecedented socioeconomic development (Hu et al., 2024; Xiao et al., 2025). Chengdu, the capital of Sichuan Province and one of western China's fastest-growing megacities, represents a prime example of such transformation. Over the past three decades, rapid population growth, industrial development, and infrastructure expansion have accelerated LCC in Chengdu (Li et al., 2024). Yet, the effects of such rapid transformations on LST remain relatively underexplored. This gap limits our understanding of how urban growth reshapes local thermal environments in fast-developing cities (Wang et al., 2018). Examining the long-term relationship between LCC and LST is therefore crucial, not only for understanding the environmental consequences of urbanization but also for supporting sustainable land management, climate adaptation, and urban resilience strategies (Ullah et al., 2020; Yang et al., 2022).

Although a number of global and regional LC datasets are available, their application in complex environments is often limited (Naboureh et al., 2025). It has been widely reported that existing LC products may exhibit substantial uncertainties when used at local scales, due to differences in spatial resolution, classification schemes, or training sample representativeness (Wang et al., 2023; Li et al., 2025). These discrepancies can reduce the reliability of long-term LCC analyses, particularly when evaluating fine-scale processes such as urban expansion or intra-urban heterogeneity. To address this challenge, generating locally optimized LC datasets becomes necessary.

Recent advances in cloud computing platforms, such as Google Earth Engine (GEE) and machine learning algorithms provide powerful opportunities for environmental studies. For example, Gu et al. (2025) studied spatial and temporal variations of air pollutants in the Anhui Province within GEE. In another study, Amindin et al. (2024) investigated ecological stability under LCC using GEE and machine learning algorithms. These examples highlight the reliability of cloud-based platforms to handle large volumes of satellite data and apply advanced analytical methods efficiently.

Machine learning classifiers have been widely applied in LC mapping, with Random Forest (RF) being one of the most commonly used methods due to its robustness in handling noisy and limited data. Support Vector Machines (SVM) have also demonstrated strong performance, while algorithms such as Extreme Gradient Boosting (XGB) have shown powerful predictive capability. However, the classifier that achieves the highest accuracy often varies depending on the characteristics of the study area (Naboureh et al., 2021). A major challenge is that a single classifier may struggle with the complexity of remote sensing data, where LC classes frequently overlap spectrally and exhibit high spatial variability. To address these challenges, ensemble learning is often preferred over individual classifiers, as it leverages the strengths of multiple models to produce more accurate and stable results. By combining the outputs of different classifiers (or multiple versions of the same classifier), ensemble methods can reduce bias, minimize variance, and lower the risk of overfitting, ultimately leading to more reliable LC maps across diverse and heterogeneous landscapes (Ebrahimy et al., 2022).

This contribution has been peer-reviewed. The double-blind peer-review was conducted on the basis of the full paper.
https://doi.org/10.5194/isprs-annals-X-4-W8-2025-563-2026

In this study, we investigate the spatiotemporal relationship between LCC and LST in Chengdu City from 1990 to 2020 using multi-temporal Landsat satellite data, GEE, and ensamble machine learning. The present work is planned to cover the following objectives: (i) generate high-accuracy LC maps for Chengdu, (ii) retrieve LST data at 30 m resolution, and (iii) analyse the historical trends of LCC, LST, and their interactions over the past three decades.

2. Study Area and Data

2.1 Study Area

Chengdu city (102.540–104.530°E, 30.050–31.260°N), covering an area of approximately 14,335 km², is the capital of Sichuan Province and the largest city in western China (Figure 1). Chengdu is known for its pleasant climate, strategic geographical location, and rich cultural heritage. Chengdu functions as the political, cultural, economic, and international exchange hub of Sichuan Province. The city lies in the Sichuan Basin, with a terrain characterized by low-lying central areas surrounded by higher elevations. The region has a subtropical monsoon climate marked by frequent calm winds, with mean annual precipitation ranging from 798.3 to 1541.0 mm and a mean annual temperature of 16 °C (Sun et al., 2024).

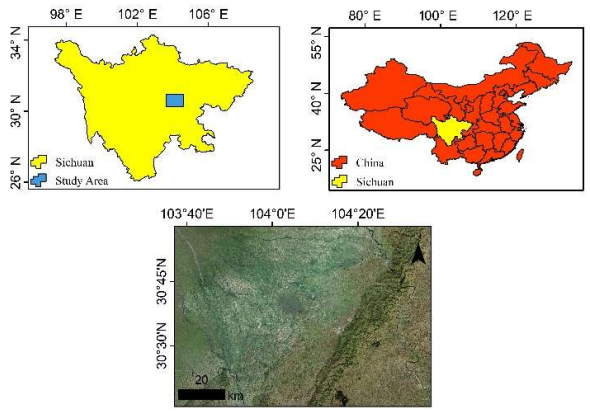

Figure 1. Location of study area

2.2 Data Collection

This study employed multi-temporal remote sensing data from Landsat sensors 5-TM, 7-ETM+, and 8-OLI to analyze LCC and LST variations in the study area between 1990 and 2020. More specifically, Landsat surface reflectance data at ten-year intervals (1990, 2000, 2010, and 2020) were acquired between January 1 and December 31 within GEE cloud computing platform. Then, for each reference year, acquired images followed by necessary pre-processing steps such as shadow removal.

3. Methodology

3.1 LC Classification

In this study, we adopted a LC classification system consisting of seven major classes: Forest, Built-up, Cropland, Bare land, Grassland, Water, and Wetland. Since the study area does not contain permanent snow or ice, this category was excluded from the classification scheme. To generate consistent LC maps across multiple time periods, we employed a sample training workflow based on the approach of Moharrami et al. (2025). High-quality reference samples were initially collected for the year 2020 through a combination of field surveys and visual interpretation of high-resolution imagery. These samples were then transferred to the target years (1990, 2000, and 2010), ensuring sufficient high-quality training samples. This approach allowed us to maintain a spatially balanced and high-quality reference dataset. For each study year, we compiled more than 800 representative samples. The dataset was randomly divided into 70% for training and 30% for validation.

To improve class separability, the classification process incorporated not only raw spectral bands but also a combination of spectral indices (Table 1) and topographic variables. The selected spectral indices included: Normalized Difference Vegetation Index (NDVI), Normalized Difference Built-up Index (NDBI), Modified Normalized Difference Water Index (MNDWI), and Enhanced Vegetation Index (EVI). Additionally, topographical data (slope, elevation, and aspect) derived from the DEM were integrated to improve discrimination between spectrally similar classes.

Index	Formula
NDVI	$\frac{NIR - R}{NIR + R}$
EVI	$2.5 \times (\frac{NIR - R}{NIR + 6 \times R - 7.5 \times B + 1})$
MNDWI	$\frac{Green - SWIR1}{Green + SWIR1}$
NDBI	$\frac{SWIR1 - NIR}{SWIR1 + NIR}$

Table 1. Spectral Indices used in this study

Previous research has demonstrated that ensemble classifiers generally outperform single classifiers in LC classification tasks by leveraging complementary strengths of individual algorithms (Ebrahimy et al., 2022). Building on this, we implemented an ensemble classifier that integrates XGB, RF, and SVM within the GEE platform. This combination enhances classification stability and accuracy, especially in heterogeneous landscapes where single classifiers may struggle to generalize effectively. The performance of the classification results was evaluated using common accuracy metrics, including Overall Accuracy (OA), User's Accuracy (UA), Producer's Accuracy (PA), and the F1-score. These metrics provide a comprehensive evaluation of classification quality by accounting for both omission and commission errors across classes.

3.2 Estimation of LST

The estimation of LST in this study followed the mono-window algorithm, which has been widely applied in previous works (Ding & Shi, 2013; Imran et al., 2022). The algorithm utilized thermal bands from different Landsat sensors: Band 6 from Landsat 5 and Band 10 from Landsat 8. The first step involved converting the raw digital number (DN) values from the thermal bands into spectral radiance (Lλ). For Landsat 5, this was calculated using Eq. (1), whereas for Landsat 8, Eq. (2) was applied. In both cases, the resulting Top-of-Atmosphere (TOA) radiance values were expressed in watts per square meter per steradian per micrometre ($W \cdot m^{-2} \cdot sr^{-1} \cdot \mu m^{-1}$).

$$L_\lambda = \left(\frac{L_{max} - L_{min}}{QCA_{max} - QCAL_{min}}\right) * (QCAL - QCAL_{min}) + L_{min} \quad (1)$$

Where, Lλ = spectral radiance, Lmax = the highest spectral radiance (15.303 for Landsat 5), Lmin = the lowest spectral radiance (1.238 for Landsat 5), QCALmax = highest DN (255), QCALmin = lowest DN (1), and QCAL= DN of Band 6.

This contribution has been peer-reviewed. The double-blind peer-review was conducted on the basis of the full paper.
https://doi.org/10.5194/isprs-annals-X-4-W8-2025-563-2026 | © Author(s) 2026. CC BY 4.0 License.

$$L\lambda = M_L * QCAL + A_L \quad (2)$$

Where, Lλ = spectral radiance, ML= multiplicative rescaling factor (0.0003342), QCAL= DN of Band 10, and AL = additive rescaling factor (0.1).
The second step is to convert spectral radiance into brightness temperature (B_T) using Eq. (3).

$$B_T = \frac{k_2}{\ln\left(\frac{k_1}{L_\lambda}+1\right)} \quad (3)$$

Where, B_T = brightness temperature, K_1 and K_2 = calibrated constants that differ based on sensors (for Landsat 5 K_1 and K_2 are 607.76 and 1260.56 respectively; for Landsat 8 K_1 and K_2 are 774.8853 and 1321.0789 respectively), and Lλ= spectral radiance.
Finally, the LST of the study area was calculated by emissivity (ε) correction using the brightness temperature obtained in the previous step. Furthemore, the emissivity corrected LST was calculated following Artis and Carnahan (1982) and using Eq. (4). Further, the emissivity was calculated using NDVI values of the image pixel, which depends upon the LC characteristics.

$$T_s = \frac{B_T}{1+\left(\lambda*\frac{B_T}{\rho}\right)\ln\varepsilon} - 273.15 \quad (4)$$

Where T_s is the earth's surface temperature (°C), B_T is the brightness temperature, λ is the wavelength, ρ is 1.438×10^{-2} mk, and ε is emissivity (0.97-0.99). Following Sobrino et al. (2004), pixel emissivity was written as:

$$\varepsilon = 0.004Pv + 0.986 \quad (5)$$

Here, Pv = Vegetation Proportion, and Pv was estimated using Eq. (6).

$$P_V = \left(\frac{NDVI - NDVI_{min}}{NDVI_{max} - NDVI_{min}}\right)^2 \quad (6)$$

4. Results and Discussion

4.1 LC Classification

A consistent time-series of four LC maps at 30-m resolution was produced for Chengdu city covering the period 1990–2020 at decadal intervals (Figure 2). In 2020, the landscape was dominated by Cropland, which accounted for approximately 87% of the study area, followed by Built-up land, representing about 8%. The accuracy assessment of the generated maps demonstrated an average overall accuracy of 91% across all classification years. Similarly, the average F1-score exceeded 85% for all LC classes, confirming the robustness and reliability of the classification results. Among individual classes, the Water category achieved the highest accuracy (97%), owing to its clear and distinct spectral response. In contrast, Grassland recorded the lowest accuracy with an F1-score of approximately 85.5%, a result that can be attributed to its spectral similarity with other vegetation-dominated categories, particularly cropland (Moharramy et al., 2025). The high accuracy of the generated LC maps, particularly the strong F1-score values for both minority and majority classes, demonstrates the effectiveness of the proposed framework, which integrates GEE, ensemble learning, and sample migration. This workflow provides a robust and scalable approach that can be applied in future LC classification studies. This finding is consistent with Ebrahimy et al. (2022), who highlighted the robustness of ensemble learning in LC mapping. Our results also support Moharrami et al. (2025), who demonstrated that migrating sample data is an effective approach to address the shortage of high-quality samples for long-term LC mapping.
Analysis of LCC between 1990 and 2020 reveals significant transformations in the study area. Overall, the landscape experienced a clear trend of urban expansion and agricultural intensification, with Cropland and Built-up dominating the changes (Figure 3). Cropland was the most dynamic class, experiencing both substantial gains and losses. A large area of cropland remained unchanged (4949.26 sq km), while notable portions of Forest (37.64 sq km) were converted to Cropland, indicating ongoing agricultural expansion. Built-up class also increased, primarily at the expense of Cropland and Grassland, reflecting urbanization. In contrast, Bare land and Wetlands showed minimal change, representing the classes with the lowest transitions. Forest areas experienced moderate losses, mostly to Cropland, while Water bodies and Grasslands displayed mixed transitions with smaller net changes. Overall, the LC dynamics highlight a landscape dominated by human-driven transformations, particularly urban growth and agricultural expansion, while natural or less disturbed classes such as Bare land and Wetlands remain relatively stable.

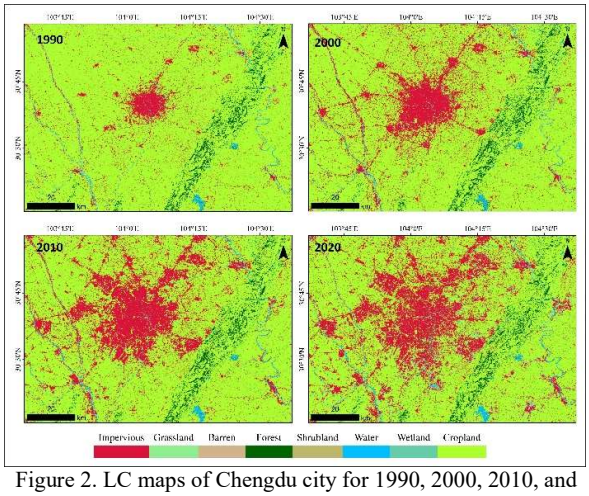

Figure 2. LC maps of Chengdu city for 1990, 2000, 2010, and 2020.

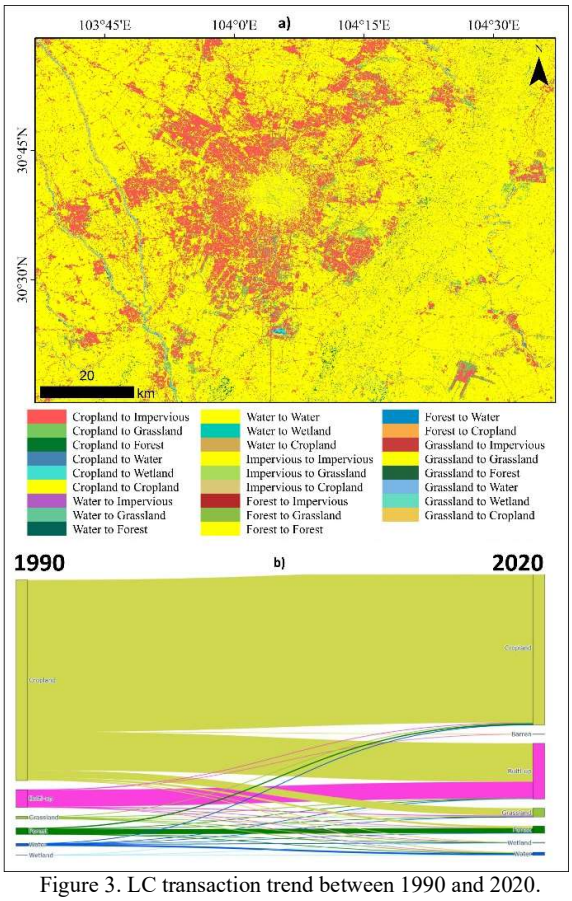

Figure 3. LC transaction trend between 1990 and 2020.

4.2 Historical LST Variations

Figure 4 presents the mean estimated Land Surface Temperature (LST) for the study area in 1990, 2000, 2010, and 2020. The analysis of Land Surface Temperature (LST) between 1990 and 2020 shows notable temporal variability. The mean LST remained stable at 26.27°C from 1990 to 2000 but increased sharply to 31.86°C by 2010, indicating a warming trend during this period. By 2020, the mean LST dropped to 23.69°C, suggesting a cooling phase in the last decade (Figure 5).

Maximum LST values peaked in 2010 at 40.53°C, while minimum temperatures were lowest in 2020 at 17.4°C. The overall pattern indicates that the study area experienced a significant warming trend between 2000 and 2010, followed by a subsequent cooling trend by 2020. These fluctuations may reflect the combined effects of land cover changes, urban expansion, and seasonal or climatic variability over the 30-year period.

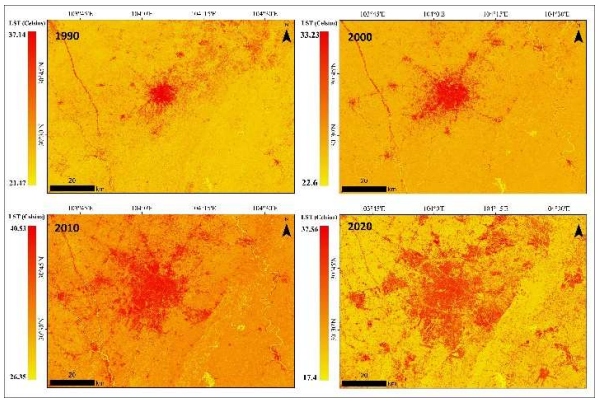

Figure 4. Estimated annual LST for the study area in 1990, 2000, 2010, and 2020.

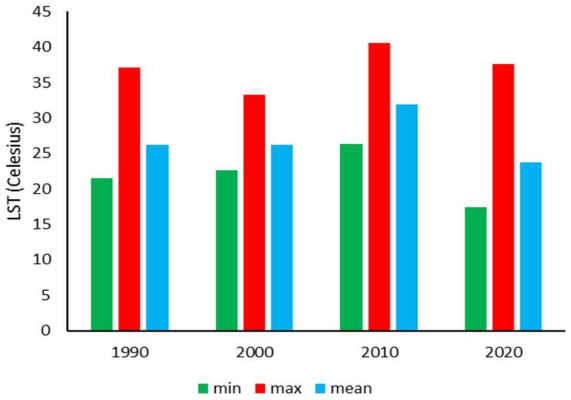

Figure 5. Temporal changes in minimum, maximum, and mean LST values between 1990 and 2020.

4.3 Impact of LCC on LST

In this study, we also used zonal statistical analysis to examine LST values across different LC classes (Table 2). In the year 2020, Bare land and Built-up areas exhibited the highest mean LSTs, 32.49°C and 28.21°C respectively, reflecting their strong heat-retaining characteristics due to sparse or absent vegetation. Grasslands also showed relatively high temperatures (27.19°C). In contrast, water bodies (20.33°C) and forests (21.20°C) recorded the lowest mean LSTs, highlighting their natural cooling effect. Wetlands (22.24°C) and croplands (22.14°C) had moderate mean temperatures, influenced by partial vegetation cover and soil exposure. This finding aligns with the results of Patel et al. (2024), who observed elevated LST values in Built-up and Bare land classes, while Water bodies and Green vegetation exhibited comparatively lower LST values in Doha, Qatar.

LC type	LST		
	Min	Max	Mean
Impervious	17.44	37.78	28.21
Grassland	17.45	37.37	27.19
Barren	24.99	36.57	32.49
Forest	17.44	35.32	21.2
Water	17.28	34.35	20.33
Wetland	17.6	35.19	22.24
Cropland	17.45	36.91	22.14

Table 2. Zonal statistical analysis of LST across different LC types in 2020.

A visual assessment of the Xinlong Lake area in Chengdu City (Figure 6) highlights the strong relationship between LC and LST. Areas dominated by dense vegetation or water bodies consistently exhibit lower LST values, typically indicated by yellow tones, reflecting their capacity to regulate microclimates through evapotranspiration and high heat storage potential of water. In contrast, built-up areas display substainally higher LST values, represented by red tones, which can be attributed to the prevalence of impervious surfaces such as concrete and asphalt that absorb and retain heat. This striking contrast clearly demonstrates the significant influence of LC type on the spatial distribution of surface temperatures, with vegetation and water functioning as natural cooling elements that mitigate localized warming. Moreover, the observed pattern provides strong evidence of the urban heat island effect, where the replacement of natural landscapes with built-up structures intensifies heat accumulation. These results underscore the critical role of green and blue infrastructure in maintaining thermal comfort and reducing surface temperature extremes in rapidly urbanizing environments.

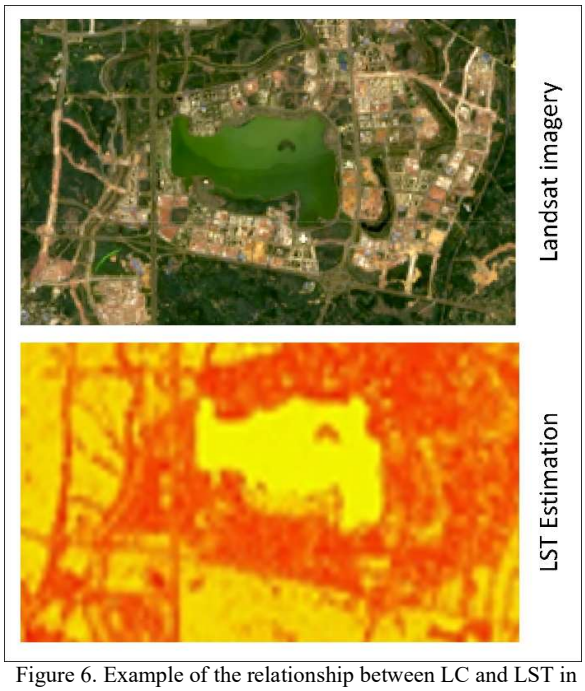

Figure 6. Example of the relationship between LC and LST in the Xinlong Lake area.

Figure 7 illustrates a notable LCC in Chengdu city. In 2010, the area was predominantly covered by grassland and cropland, providing relatively stable and cooler surface temperatures. By 2020, however, this same area had been converted into an airport, replacing vegetated surfaces with extensive impervious materials such as asphalt and concrete. This transformation corresponds to a substantial increase in LST, clearly demonstrating how LCC can amplify local thermal conditions through the reduction of natural cooling processes and the intensification of heat storage. Such changes not only alter the local microclimate but also contribute to the broader urban heat island effect. These observations underscore the critical role of LC dynamics in driving LST variability and highlight the necessity of incorporating LC considerations into urban planning, climate adaptation strategies, and sustainable environmental management practices.

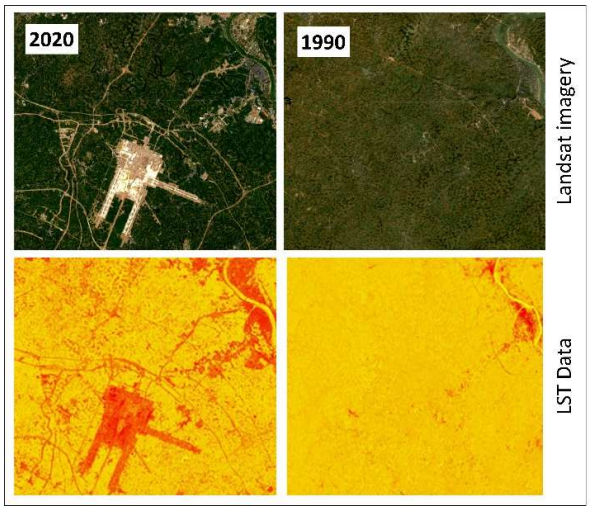

Figure 7. LC transformation at Tianfu Airport between 1990 and 2020 and its impact on LST.

5. Conclusion

This study demonstrates how intense LCC over the past three decades have reshaped the thermal environment of Chengdu City. The integration of satellite remote sensing, machine learning, and reference data migration proved effective in producing accurate, high-resolution LC maps, enabling reliable assessments of LST dynamics. The findings confirm that urban expansion and agricultural intensification are the dominant forces behind both LCC and LST variability, with Built-up and Bare land areas amplifying surface heating while Vegetation and Water consistently mitigate it. Importantly, the temporal trajectory of LST highlights the sensitivity of local climate conditions to shifts in LC composition. Beyond offering empirical evidence of these interactions, this research provides a practical methodological framework for long-term LC monitoring, with direct implications for urban planning, agricultural management, and climate adaptation strategies.

Acknowledgements

This work was supported by the Sichuan province key research and development project under Grant 2023YFWZ0007.

References

Amindin, A., Siamian, N., Kariminejad, N., Clague, J.J., Pourghasemi, H.R., 2024: An integrated GEE and machine learning framework for detecting ecological stability under land use/land cover changes. *Global Ecology and Conservation*, 53, e03010. doi.org/10.1016/j.gecco.2024.e03010

Artis, DA., Carnahan, WH., 1982: Survay of emissivity variability in thermography of urban areas. *Remote Sensing of Environment*, 12(4), 313-329. doi.org/10.1016/0034-4257(82)90043-8

Ding, H., Shi, W., 2013: Land-use/land-cover change and its influence on surface temperature: a case study in Beijing City. *International Journal of Remote Sensing*, 34(15), 5503-5517. doi.org/10.1080/01431161.2013.792966

Ebrahimy, H., Mirbagheri, B., Matkan, A.A., Azadbakht, M., 2022: Effectiveness of the integration of data balancing techniques and tree-based ensemble machine learning algorithms for spatially-explicit land cover accuracy prediction. *Remote Sensing Applications: Society and Environment*, 27, 100785. doi.org/10.1016/j.rsase.2022.100785

Firozjaei, M.K., Kiavarz, M., Alavipanah, S.K., Lakes, T., Qureshi, S., 2018: Monitoring and forecasting heat island intensity through multi-temporal image analysis and cellular automata-Markov chain modelling: A case of Babol city, Iran. *Ecological Indicators*, 91, 155-170. doi.org/10.1016/j.ecolind.2018.03.052

Gómez, C., White, J.C., Wulder, M.A., 2016: Optical remotely sensed time series data for land cover classification: A review. *ISPRS Journal of Photogrammetry and Remote Sensing*, 116, 55-72. doi.org/10.1016/j.isprsjprs.2016.03.008

Gu, H., Zhang, W., 2025: Quantitative assessment of urban-rural spatiotemporal heterogeneity in air pollutants using GEE multi-source data across the Anhui province, China. *Atmospheric Pollution Research*, 16(5), 102464. doi.org/10.1016/j.apr.2025.102464

He, Y., Liu, X., Wu, D., Li, S., Zhou, P., 2025: Ecological risks and patterns associated with land use/cover changes along the Belt and Road Initiative routes. *Land Degradation & Development*, 36(6), 2075–2094. doi.org/10.1002/ldr.5483

Hu, C., Zhang, M., Huang, G., Li, Z., Sun, Y., Zhao, J., 2024: Tracking the impact of the land cover change on the spatial–temporal distribution of the thermal comfort: Insights from the Qinhuai River Basin, China. *Sustainable Cities and Society*, 116, 105916. doi.org/10.1016/j.scs.2024.105916

Imran, H.M., Hossain, A., Shammas, M.I., Das, M.K., Islam, M.R., Rahman, K., Almazroui, M., 2022: Land surface temperature and human thermal comfort responses to land use dynamics in Chittagong city of Bangladesh. *Geomatics, Natural Hazards and Risk*, 13(1), 2283–2312. doi.org/10.1080/19475705.2022.2114384

Komeh, Z., Hamzeh, S., Memarian, H., Attarchi, S., Alavipanah, S.K., 2025: A remote sensing approach to spatiotemporal analysis of land surface temperature in response to land use/land cover change via cloud base and machine learning methods, case study: Sari Metropolis, Iran. *International Journal of Environmental Research*, 19(3), 98. doi.org/10.1007/s41742-025-00752-4

Li, J., He, X., Liu, Y., Zhang, C., Wu, X., Yan, D., Luan, Z., 2025: Tracking long-term wetland dynamics based on sample migration and two-stage hierarchical classification: A case study of Jiangsu Province. *Catena*, 254, 108993. doi.org/10.1016/j.catena.2025.108993

Li, Z., Zhu, J., Tian, Y., 2024: Impact of land-use–land cover changes on the service value of urban ecosystems: Evidence from Chengdu, China. *Journal of Urban Planning and Development*, 150(3), 05024028. doi.org/ 10.1061/JUPDDM.UPENG-4827

Mohammadi Foumani, N., Miller, L., Tan, C.W., Webb, G.I., Forestier, G., Salehi, M., 2024: Deep learning for time series classification and extrinsic regression: A current survey. *ACM Computing Surveys*, 56(9), 1–45. doi.org/10.1145/3649448

Moharrami, M., Attarchi, S., Gloaguen, R., Alavipanah, S.K., 2025: Evaluation of similarity-checking methods for reference samples migration to monitor land cover changes in the complex terrain of the Alborz Mountains, Iran. *Earth Science Informatics*, 18(3), 318. doi.org/ 10.1007/s12145-025-01830-z

Naboureh, A., Bian, J., Lei, G., Li, A., 2021: A review of land use/land cover change mapping in the China-Central Asia-West Asia economic corridor countries. *Big Earth Data*, 5(2), 237–257. doi.org/10.1080/20964471.2020.1842305

Naboureh, A., Li, A., Bian, J., Moharrami, M., Ebrahimy, H., Lei, G., …, Amani, M., 2025: Accuracies, discrepancies, and challenges of the 10 m global land cover products in mountains. *GIScience & Remote Sensing*, 62(1), 2556064. doi.org/10.1080/15481603.2025.2556064

Patel, S., Indraganti, M., Jawarneh, R. N., 2024: Land surface temperature responses to land use dynamics in urban areas of Doha, Qatar. *Sustainable Cities and Society*, 104, 105273. doi.org/10.1016/j.scs.2024.105273

Sobrino, JA., Jimenez-Munoz, JC., Paolini, L., 2004: Land surface temperature retrieval from LANDSAT TM 5. *Remote Sensing of Environment*, 90(4), 434-440. doi.org/10.1016/j.rse.2004.02.003

Sun, H., Sun, Y., Mu, H., Luo, J., Lin, X., Zhang, Y., 2024: Spatiotemporal changes and trends in ecological quality based on the GEE: A case study of Chengdu City, China. *Polish Journal of Environmental Studies*. doi.org/10.15244/pjoes/193146

Ullah, M., Li, J., Wadood, B., 2020: Analysis of urban expansion and its impacts on land surface temperature and vegetation using RS and GIS: A case study in Xi'an City, China. *Earth Systems and Environment*, 4(3), 583–597. doi.org/10.1007/s41748-020-00166-6

Wang, M., Mao, D., Wang, Y., Xiao, X., Xiang, H., Feng, K., Wang, Z., 2023: Wetland mapping in East Asia by two-stage object-based Random Forest and hierarchical decision tree algorithms on Sentinel-1/2 images. *Remote Sensing of Environment*, 297, 113793. doi.org/10.1016/j.rse.2023.113793

Wang, S., Ma, Q., Ding, H., Liang, H., 2018: Detection of urban expansion and land surface temperature change using multi-temporal landsat images. *Resources, Conservation and Recycling*, 128, 526-534. doi.org/10.1016/j.resconrec.2016.05.011

Xiao, W., Ruan, L., Wang, K., Xu, S., Yue, W., He, T., Zhang, Y., 2025: Measuring three-dimension urban expansion using multi-source data and change detection algorithm: A case study of Shanghai. *Cities*, 158, 105682. doi.org/10.1016/j.cities.2024.105682

Yang, L., Li, X., Shang, B., 2022: Impacts of urban expansion on the urban thermal environment: a case study of Changchun, China. *Chinese Geographical Science*, 32(1), 79-92. doi.org/ 10.1007/s11769-021-1251-3